Evidence of partial melting beneath a continental margin: case of Dhofar, in the Northeast Gulf of Aden (Sultanate of Oman)

Clemence Basuyau, Christel Tiberi, Sylvie Leroy, G. Stuart, Ali Al-Lazki, K. Al-Toubi, C. Ebinger

Geophysical Journal International

Geophys. J. Int. (2010) **180,** 520–534 doi: 10.1111/j.1365-246X.2009.04438.x

Evidence of partial melting beneath a continental margin: case of Dhofar, in the Northeast Gulf of Aden (Sultanate of Oman)

C. Basuyau,[1]* C. Tiberi,[1]* S. Leroy,[1,2] G. Stuart,[3] A. Al-Lazki,[4] K. Al-Toubi[4] and C. Ebinger[5]

[1] *UPMC Univ Paris* 06, *UMR* 7193, *ISTEP,* F-75005, *Paris, France. E-mail: clemence.basuyau@upmc.fr*
[2] *UMR* 7193, *ISTeP, CNRS, Case* 129, 4 *place Jussieu,* 75252 *Paris Cedex* 05, *France*
[3] *School of Earth and Environment, University of Leeds, Leeds* LS2 9JT, *UK*
[4] *Department Earth Sciences, Sultan Qaboos University, Sultanate of Oman*
[5] *Department Earth and Environmental Sciences, University of Rochester, USA*

Accepted 2009 October 29. Received 2009 October 16; in original form 2009 July 10

SUMMARY

Gravity data and *P*-wave teleseismic traveltime residuals from 29 temporary broad-band stations spread over the northern margin of the Gulf of Aden (Dhofar region, Oman) were used to image lithospheric structure. We apply a linear relationship between density and velocity to provide consistent density and velocity models from mid-crust down to about 250 km depth. The accuracy of the resulting models is investigated through a series of synthetic tests. The analysis of our resulting models shows: (1) crustal heterogeneities that match the main geological features at the surface; (2) the gravity edge effect and disparity in anomaly depth locations for layers at 20 and 50 km; (3) two low-velocity anomalies along the continuation of Socotra-Hadbeen and Alula-Fartak fracture zones between 60 and 200 km depth; and (4) evidence for partial melting (3–6 per cent) within these two negative anomalies. We discuss the presence of partial melting in terms of interaction between the Sheba ridge melts and its along-axis segmentation.

Key words: Tomography; Gravity anomalies and Earth structure; Continental margin: divergent; Indian Ocean.

1 INTRODUCTION

The break-up of continents and the creation of new ocean basins are processes that have reshaped Earth's surface since Archean time. Breakup process is poorly understood, in large part because most successfully rifted passive margins formed more than 100 Ma ago, and the thermal response of the lithosphere has long since decayed. Another problem in the geophysical exploration of passive margins is the combination of signals coming from various sources (e.g. Worzel 1968). These include the drastic crustal thinning, the change of crustal nature (oceanic versus continental), the presence of deep sedimentary basins and/or the presence of seaward dipping reflectors (SDRs). In this case, most geophysical methods can hardly associate the right wavelength of the total signal with the corresponding structure (e.g. Watts & Stewart 1998). Still debated are the relative importance of magmatism and faulting in strain accommodation, and the thermal–mechanical evolution of continental lithosphere from rift onset to breakup (e.g. Buck 2004). Likewise, the along-strike variability of rift structure and its relation to mantle thermal anomalies remains poorly understood (e.g. Bastow *et al.* 2005; Lizarralde *et al.* 2007).

The Gulf of Aden extends from Africa (Djibouti) to the Indian Ocean with a N075 trend and it separates the Arabian and Somalian plates (Fig. 1). Its margins are only 400 km apart and well preserved beneath a thin postrift sedimentary cover. It then offers an ideal location to compare the along-strike structural segmentation of early syn-rift to seafloor spreading anomalies with the patterns of lithospheric thinning and heating. The Gulf of Aden evolution and its margin structure (both volcanic and non-volcanic) are closely related to the presence of the Afar plume at its western end (e.g. Manighetti *et al.* 1997; Bellahsen *et al.* 2003). It is thus an ideal place for studying the interactions between asthenosphere and lithosphere. We focus our study on the Dhofar Area (Southern Oman; Fig. 1) for two main reasons. First, it is far from any other major geodynamic processes that could interact with break-up: the Arabian subduction beneath Eurasia (Zagros and Makran) is more than 800 km away and is dipping to the north. Secondly, this region benefits from previous geophysical studies for crustal constraints (e.g. Leroy *et al.* 2004; d'Acremont *et al.* 2006; Tiberi *et al.* 2007).

In 2003 and 2005, two seismological experiments were carried out along the southern coast of Oman, in the Dhofar area. In total,

*Now at: Géosciences Montpellier, Université Montpellier II, CNRS UMR 5243, France.

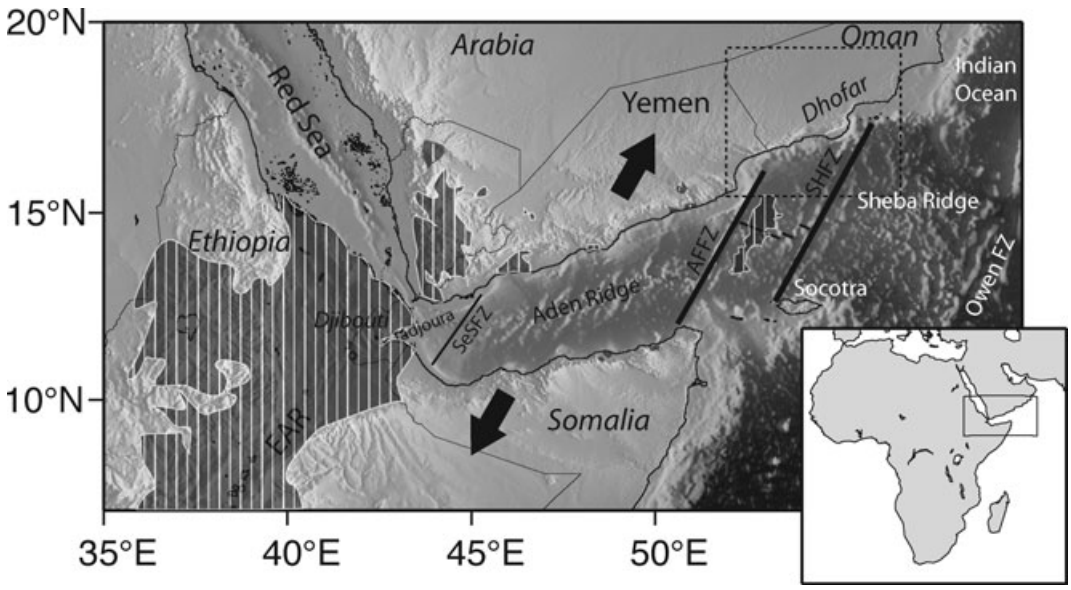

Figure 1. Simplified geodynamical map of the study region. The main structural units are named and localized (EAR, East African Rift; SeSFZ, Shukra el Sheik Fault Zone; AFFZ, Alula-Fartak Fault Zone; SHFZ, Socotra-Hadbeen Fault Zone; Owen FZ, Owen Fault Zone). The two black arrows indicate the direction of extension between Arabia and Somalia plate. The hachured areas are indicative of volcanic regions. The dashed square shows the zone where joint inversion is performed.

29 broad-band stations operated each for 1 yr, recording numerous teleseismic events. We have combined these seismological data with existing gravity data in a joint inversion scheme to estimate both *P*-wave velocity and density structure beneath the northeastern margin of the Gulf of Aden. We reach depths of 250 km with a spatial resolution of about 50 km.

We then discuss the presence of anomalous bodies in terms of interaction between mantle and crustal processes, rift evolution and margin/ridge segmentation.

1.1 Tectonic setting

Rifting of the Gulf of Aden commenced around 35 Ma. Seafloor spreading initiated by 18 Ma in the eastern Gulf of Aden, where mid-ocean ridge orientation is oblique to plate opening (N026). Its spreading rate increases from west (1.6 cm yr^{-1}) to east (2.3 cm yr^{-1}) (e.g. Fournier *et al.* 2001). Oceanic spreading started at least at 17.6 Ma in the eastern part of the Gulf (Leroy *et al.* 2004), whereas seafloor spreading in the western part seems to continue to propagate westward into the Afar depression (Manighetti *et al.* 1997; Huchon & Khanbari 2003). The onset of continental rifting coincides with the highest eruption rates of continental basaltic flood at ∼30 Ma (e.g. Courtillot *et al.* 1999; Ukstins *et al.* 2002; Wolfenden *et al.* 2004). The major discontinuity of Shukra-El Sheik (Fig. 1) may indicates the limit of the Afar hotspot influence and correspond to a major change in the rheology of the lithosphere (Hébert *et al.* 2001). West of this major discontinuity, the margins are considered volcanic (Tard *et al.* 1991), whereas they are non-volcanic east of it (e.g. Leroy *et al.* 2004; d'Acremont *et al.* 2005) (Fig. 1). However, recent evidence has been reported of both volcanic activity and high heat flow more than 1000 km east of the Afar (Lucazeau *et al.* 2008, 2009). The non-volcanic characteristic of the eastern part of the Gulf of Aden is then subject to question, and one can wonder whether hot mantle material could be still present east of the Shukra-El Sheik fracture zone.

The Shukra-El Sheik fracture zone is one of the main structures that segment the Gulf of Aden. Their orientations range from N025 to N030 (Audin *et al.* 2004). The Alula-Fartak fracture zone is a major transform fault that horizontally offsets the Sheba ridge by ∼180 km (d'Acremont *et al.* 2005). The Alula-Fartak fracture zone parallels the Socotra-Hadbeen fracture zone (SHFZ; Fig. 1). The early mid-ocean ridge coincide with the late syn-rift segmentation of the continental margins (d'Acremont *et al.* 2006).

The margins are strongly asymmetric, but they comprise the same sequences as the main Arabian platform: Cretaceous to Eocene marine platform sequences overlying Precambrian to Cambrian basement. The northern margin (Oman) is narrower and steeper than the southern one (Eastern Somalia and Socotra island). This asymmetry is linked to the existence of Jurassic basins in the Gulf of Aden, which generate strong pre-existing lithospheric fabrics (d'Acremont *et al.* 2006).

In our study area, on the northern margin (Dhofar, Oman), the pre-rift marine sequence has been evaluated from geological observations to be about 2 km thick (Roger *et al.* 1989). Several fault-bounded syn-rift basins striking from N70°E to N110°E cut all these sequences (Lepvrier *et al.* 2002; Bellahsen *et al.* 2006). The major syn-rift basins on land are Salalah and Ashawq basins in the Dhofar area. The Jabal Qara fault bounds these basins and is coincident with the localization of crustal deformation in this area (Tiberi *et al.* 2007).

1.2 Previous seismological work

Although numerous studies dedicated to the lithospheric structure beneath Arabia and its surroundings were conducted for decades, they mainly focus on the eastern, northern or western parts of Arabia (e.g. Benoit *et al.* 2003; Park *et al.* 2007). Anomalous hot mantle beneath the Arabian shield is clearly imaged down to 400 km from body wave (Knox *et al.* 1998) and surface wave tomography (Debayle *et al.* 2001; Sebai *et al.* 2006). Also, anomalous

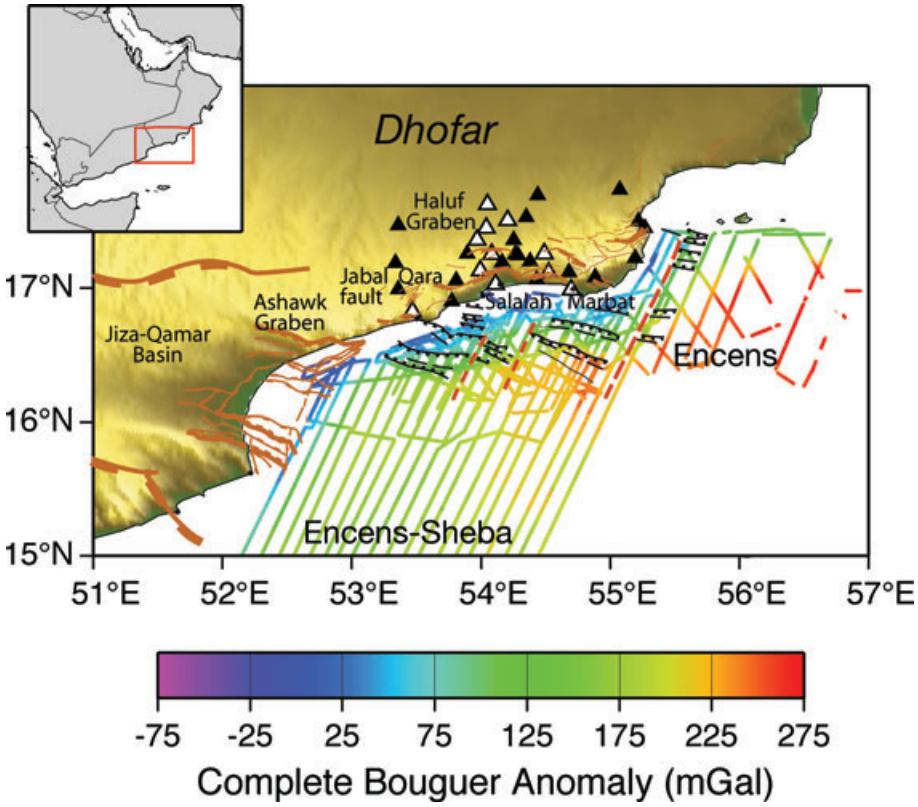

Figure 2. Complete Bouguer anomaly for the offshore part of our study region. The data are collected from two geophysical cruises: Encens-Sheba (Leroy *et al.* 2004) and Encens (Leroy *et al.* 2006). The two seismological temporary networks associated to this work are represented by the white (2003–2004) and black (2005–2006) triangles. Brown and black continuous segments underline onland and offshore main faults, respectively. Brown dashed lines offshore indicate major segmentation of the northern Aden margin (from d'Acremont *et al.* 2005).

potentially hot lithospheric mantle is indicated by low Pn velocities along the Red Sea passive margin (Al-Lazki *et al.* 2004), and indicated by inefficient Sn propagation beneath the Gulf of Aden and the Red Sea (Al-Damegh *et al.* 2004). The thickness and structure of the crust and the lithosphere are known through the Arabian plate (e.g. Hansen *et al.* 2006; Al-Lazki *et al.* 2002). Al-Damegh *et al.* (2005) deduced the average crustal thickness of the late Proterozoic Arabian shield as 39 km. In the northern part of the Arabian platform, the crust varies from 33 to 37 km; however, the crust is thicker (41–53 km) in the southeastern part of the platform (Al-Lazki *et al.* 2002). Along the Red Sea, the crust thins to about 23 km (Al-Damegh *et al.* 2005). Hansen *et al.* (2006) deduce from shear-wave splitting the presence of a density-driven flow associated with the channelized Afar upwelling.

The lithospheric structure of the Gulf of Aden margins remains poorly constrained. Surface wave tomography produces low resolution (∼1000 km) images of the upper mantle part only (Debayle *et al.* 2001; Sebai *et al.* 2006). In 2003, the first seismological experiment carried out in the Dhofar area gave insight to the Moho variations across the northern margin of the Gulf of Aden from receiver function analysis (Tiberi *et al.* 2007). This study showed (1) a crustal thinning from 35 km beneath the northern rift flank to 26 km beneath the Salalah coastal plain and (2) a localization of the crustal thinning below the first known tilted block of the margin. Crustal thinning is more pronounced beneath the pre-rift basins, suggesting pre-rift structural variations influenced the Oligocene–Pliocene rifting. This work has been strengthened and completed by offshore geophysical surveys in the past few years (Leroy *et al.* 2004, 2006; d'Acremont *et al.* 2005, 2006; Lucazeau *et al.* 2008).

2 DATA PREPARATION

To image the lithospheric structure of the northern margin in the Gulf of Aden, we used two data sets that joined in a common inversion scheme. Gravity data gives more information on crustal structure, whereas teleseismic data provides a better resolution below 40 km.

2.1 Gravity data

The first data set is the complete Bouguer anomaly map for the Dhofar region (Sultanate of Oman). The continental part of the data is a compilation of confidential values (by courtesy of the Ministry of Commerce and Industry of Sultanate of Oman), whereas marine data were collected during the Encens-Sheba (Leroy *et al.* 2004) and Encens (Leroy *et al.* 2006, 2009b) cruises (Fig. 2).

The complete Bouguer anomaly was computed using an average density of 2670 kg m^{-3} for topographic loads and slab correction. Water density value was set to 1030 kg m^{-3}.

We use intitial terrestrial and marine gravity data sets. After combining and decimating these two data sets, we use 23 746 Bouguer anomaly measurements. The final data set shows that the values are ranging from −70 to 290 mGal. The complete Bouguer anomaly presents a long wavelength gradient perpendicular to the coast with

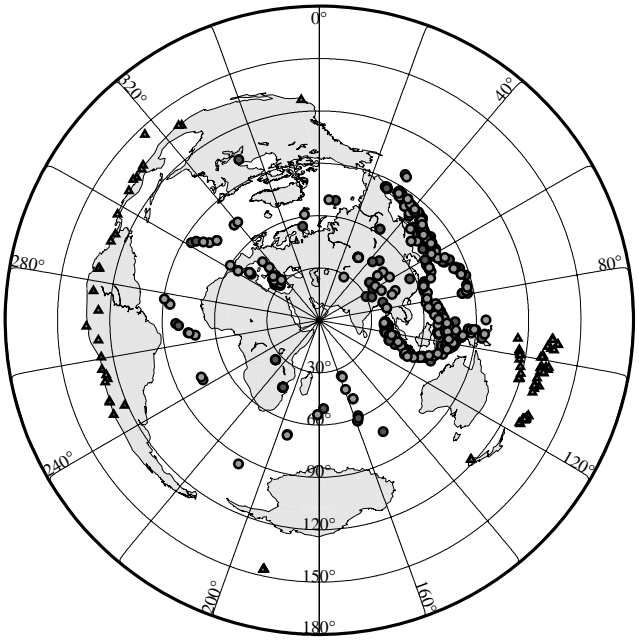

Figure 3. Azimuthal distribution of earthquakes used in this study. The circles represent events arriving with a first *P*-wave, whereas the triangles represent events arriving with a first *PKP* phase.

negative to positive values from continental to oceanic domain, respectively. A shorter wavelength component can be observed offshore along the coast, corresponding to a late syn-rift, high strain rift system characterized by tilted blocks imaged in seismic reflection data (d'Acremont *et al.* 2005). This component has a high amplitude.

2.2 Seismological data

The seismological data comes from two temporary broadband networks deployed in 2003 and 2005 in the framework of a collaborative project between France (CNRS, Univ. Paris 6), UK (Leeds and Royal Holloway University of London) and Oman (Univ. Sultan Qaboos and the Directorate of Minerals).

Eleven stations were first deployed in March 2003 for one full year (French Margins Program). The sensors were Guralp 3-component CMG-40TDs with a natural period of 30 s, recording with a sampling rate of 50 s.p.s. Then, 19 new stations were deployed from September 2005 to August 2006 (NERC project). All sensors were Guralp 3 components, either of CMG40 or CMG6 type (50 s.p.s., natural period of 30 s). Fig. 2 shows a location map of the broadband stations used for earthquake observations in Salalah region during the Dhofar Seismic Experiment. We only consider events in the epicentral distance range from 30° to 150° with a clear *P* or *PKP* phase. About 180 events in 2003 and more than 240 events for 2005 of magnitude greater than 5.0 were finally selected and used in the analysis. Fig. 3 shows the geographic distribution of the selected teleseismic events.

The final seismological data set was composed of 4989 *P* and *PKP* delay times calculated using IASP91 reference Earth model (Kennett & Engdahl 1991). They range between −0.9 and +0.9 s. As the arrival times were determined from waveform cross-correlation (VanDecar & Crosson 1990), we could assign a small picking error for each residual within the range ±0.01 to ±0.15 s.

Table 1. Initial parametrization for the joint inversion.

Layer	Depth range (km) for		V_P	Density
	Density blocks	Velocity nodes	(km s^{-1})	(g cm^{-3})
1	0–20	0	5.0	2.67
2	20–50	40	7.0	2.67
3	50–75	60	7.4	3.1
4	75–105	90	8.0	3.2
5	105–135	120	8.0	3.3
6	135–160	150	8.0	3.3
7	160–185	170	8.1	3.3
8	185–230	200	8.2	3.3

3 METHOD

To simultaneously invert both of the relative delay times and the gravity data in the Gulf of Aden, we applied a joint inversion in the sense of Lines *et al.* (1988) and Lees & VanDecar (1991). In this scheme, velocity and density variations (ΔV and $\Delta\rho$, respectively) are linked with a linear relationship taken from Birch (1961)

$$\Delta V_p = B \times \Delta\rho,$$

where B can range between 2 and 5 km s^{-1} g^{-1} cm^3, depending on rock types (Birch 1961), pressure and temperature conditions (Christensen & Mooney 1995).

The used method was initiated by Zeyen & Achauer (1997) and then developed by Jordan & Achauer (1999) and Tiberi *et al.* (2003). In this method, in addition to velocity and density perturbations we can also consider the B coefficient as an inversion parameter which varies with depth. Its variations only reflect its statistical and pressure dependant variations. However, to keep the coupling between velocity and density, we maintain it into a reasonable range of values by fixing its standard deviation σ very low. We solve this highly non-linear problem with an iterative least-squares method based on a Bayesian approach (Zeyen & Achauer 1997). Thus, any *a priori* information can be introduced to reduce the set of possible solutions (σ, smoothing, model geometry, ...).

As the method and parametrization are extensively presented elsewhere (Zeyen & Achauer 1997; Tiberi *et al.* 2003), we only give hereafter short insights on our initial model organization. The density variations are distributed into rectangular blocks (Blakely 1995), whereas velocities are calculated on nodes with an interpolation between each of them (Thurber 1983). For this study, we have selected a model composed of eight layers distributed from the surface down to 230 km (Table 1). Each layer is divided into 15 density blocks and 22 velocity nodes in the east–west axis and 13 blocks and 23 nodes in the north–south axis. The density block size varies from 15 to 50 km and the lateral spacing between nodes ranges from 10 to 100 km. We start with homogeneous layers and we link velocity and density variations through an average B value of 3 km s^{-1} g^{-1} cm^3 for each layer. The initial values for density and velocity are summed up into Table 1, based on usual values for those parameters at those depths. We assigned initial standard deviation for each parameter: 0.01 km s^{-1}, 0.005 g cm^{-3} and 0.1 km s^{-1} g^{-1} cm^3 for velocity, density and B factor, respectively. We considered constant standard deviations to take into account the lack of information on the depth location of structures. Velocity nodes are constrained and inverted if more than five teleseismic rays pass in their vicinity.

After several trials, the smoothing parameter has been selected as 0.001 for both the density and velocity, which allows for a good balance between realistic contrasts and mild spatial variations. This

value limits the short wavelengths, which could lead to incoherent results and unstable inversion.

Recent receiver function analysis gives *a priori* crustal thickness estimations beneath some of our stations (Tiberi *et al.* 2007). However, there are two difficulties which prevents us from using this *a priori* information in our inversion. First this information is very sparse and unevenly distributed. Secondly, the joint inversion uses a 3-D raytracing and an iterative scheme which prevents from integrating *a priori* crustal delay time estimation from the receiver function. We thus consider the upper and lower crust to be about 40 km thick together and represented by the first two layers of the model (Table 1). The Moho variations will then appear as density and velocity variations within those two layers.

4 RESULTS

To estimate the resolution of our joint inversion, a series of synthetic tests have been performed. To start with, we create a fictitious Earth model with known density and velocity perturbations (synthetic model). The density and velocity perturbations are linked following a Birch type law. Then through this model we compute the seismic traveltime residuals and the gravity anomaly for the actual rayset and gravity data geometry, respectively (synthetic data set). Finally, we inverted the synthetic data in the same manner as the actual inversion (same homogeneous starting model, same smoothing, same data distribution and standard deviation parameters).

4.1 Checkerboard test

To assess the resolving power of the joint inversion technique, we first analysed the ability of our ray geometry and gravimetric anomaly calculations to retrieve a standard checkerboard model. The checkerboard approach is a classic test to highlight areas of good ray coverage, to estimate the extent to which smearing of anomalies is occurring, and to evaluate the shortest wavelength of the anomaly that can be resolved with our seismic ray geometry.

In this test, we alternated the positive and negative perturbations in both velocity and density models throughout layers 3, 4 and 8. The initial variation is set to ± 5 per cent for the velocity, resulting in density perturbation of ± 0.16 g cm^{-3}. The perturbations concern two adjacent density blocks and the velocity nodes included within them. Fig. 4 depicts the recovered velocity and density structures from the inversion of this checkerboard geometry. The density perturbing bodies are better retrieved in the shallowest layer of the model both in location and amplitude and are fairly close to the initial perturbations. At greater depth, the initial density anomalies are poorly recovered because of the rapid decay of gravity amplitude with distance. These results represent a weak density resolution for depths greater than 100 km.

The recovered velocity structure from the checkerboard test shows that the perturbing blocks are clearly distinct from one to another, indicating a fairly good lateral resolution. As classically observed, for teleseismic traveltime inversion, the velocity perturbations are better retrieved in the deepest part of the model than in the shallowest layers, where more rays cross. Besides, in general, the resolution of the velocity increases with depth from the edges to the centre of the array (Evans & Achauer 1993). Furthermore, the initial perturbations are better located south–east of the study area with a maximum perturbation of ± 2.5 per cent (about half the input anomaly). This is due to the high density of rays originating from the Pacific subduction zones (Fig. 3). Note that at the edges of the array, the input anomalies show evidence of streaking due to the lack of crossing rays.

We estimate from this test that about 50 per cent of the initial amplitude for the velocity anomalies were recovered. This is partly caused by the vertical (upward and downward) smearing of the velocity anomalies (Fig. 4c). This effect is common in all teleseismic analysis and is due to the smearing of the velocity anomalies along the nearly vertical ray paths.

In order to clarify our interpretation, we hereafter subdivided the results section into two parts: the first one represents the crustal structure for both the density and velocity models while the second one deals with the upper mantle part of the models. The velocity and density models presented hereafter (Figs 6 and 7) result from 5 iterations. The good convergence is indicated by the total decrease of the root mean square (RMS) through the five iterations (Fig. 5) and is favoured by the standard deviation value we impose to the B factor (0.1 km s^{-1} g^{-1} cm^3). The overall decrease of the RMS is 94.3 per cent and 55.5 per cent for the gravity and delay time data, respectively. The reduction of the total residual sum in our case is more than 90 per cent (data, parameter, and smoothing constaint). Besides, the final standard deviations for the calculated data are 93.373 mGal and 0.175 s for gravity anomalies and delay times respectively, very close to the observed data (93.567 mGal and 0.203 s). The final density and velocity variations range between -0.6 g cm^{-3} and $+0.6$ g cm^{-3}, and -6 per cent and $+6$ per cent respectively, indicating reasonable values for lithospheric scale.

When comparing the computed gravity from the density model with the observed data, only very short wavelength differences appear (± 50 mGal). It clearly reflects a good agreement between our model and data. The short wavelength residuals are directly related to our coarse grid size compared to the smallest crustal structures. Furthermore, the highest residual values correspond to areas where we anticipate large lateral variations in crustal structure: tilted blocks and sediment-filled rift basins along the coast, the Jabal Qara fault or the Socotra-Hadbeen fracture zone (see Figs 1 and 2 for location names).

4.2 Crustal structure

The crust is contained within the two first layers of our models (from 0 to 50 km, Fig. 6). Within those layers, the obtained resulting contrasts are in the range of ± 0.6 g cm^{-3} for the density and ± 6 per cent for the velocity perturbations. Those upper crustal anomalies are related to geological structures observed at the surface: the low velocity/low density anomaly at the centre of the network corresponds to the 3 km of sediments deposited in the Salalah basin, whereas the western low corresponds to the Ashawk basin depocentre. The positive anomaly located beneath the easternmost stations of the network correlates with the Precambrian basement exposure along the margin following the footwall of the Mirbat escarpment where pre-rift sedimentary cover is absent.

In contrast, velocity and density models are clearly inconsistent for layer 2 (20-50 km)(Fig. 6). We notice the presence of very low density anomalies running along the coast which are not related to any low velocity anomalies. The seismic ray coverage in this part of the model is not dense enough to clearly image the associated offshore velocity structures (see synthetic test; Fig. 4). The observed low-density patterns could be the signature of the deep and numerous sedimentary basins present along the coast (d'Acremont *et al.* 2006). However, the joint inversion clearly misjudges their depth estimation in the density model by locating them too deep.

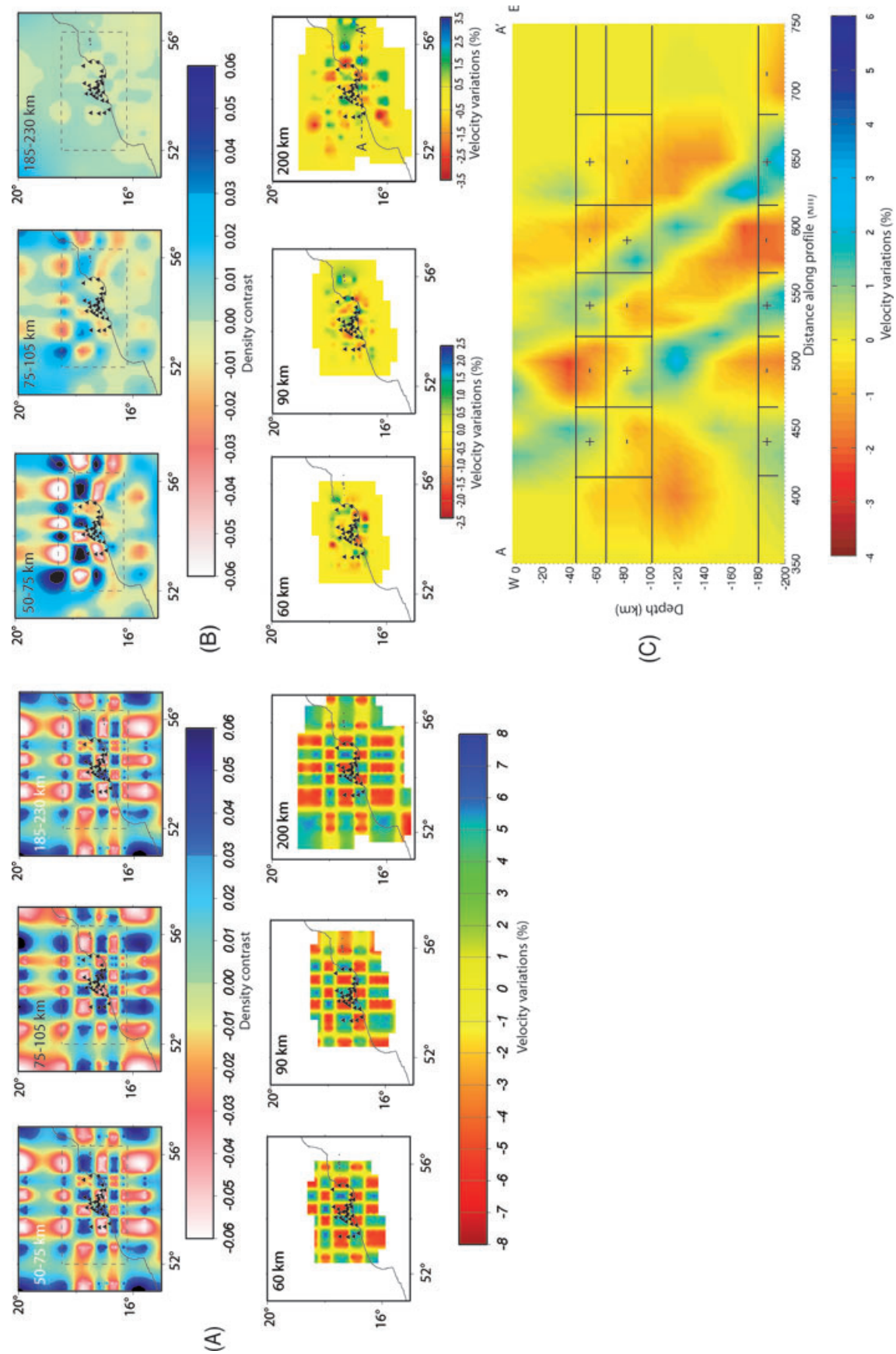

Figure 4. Checkerboard test for the joint inversion of gravity and seismological data. (a) Synthetic input model for density (top) and *P*-wave velocity (bottom), (b) depth slices through the retrieved density (top) and velocity (bottom) models. (c) Cross-section along the AA' profile whose location is indicated by the dashed line on the slice at 200 km on (b). The ± boxes on the cross-section are indicative of input velocity perturbations location. The dashed box on density slices indicates the limits of the gravity data.

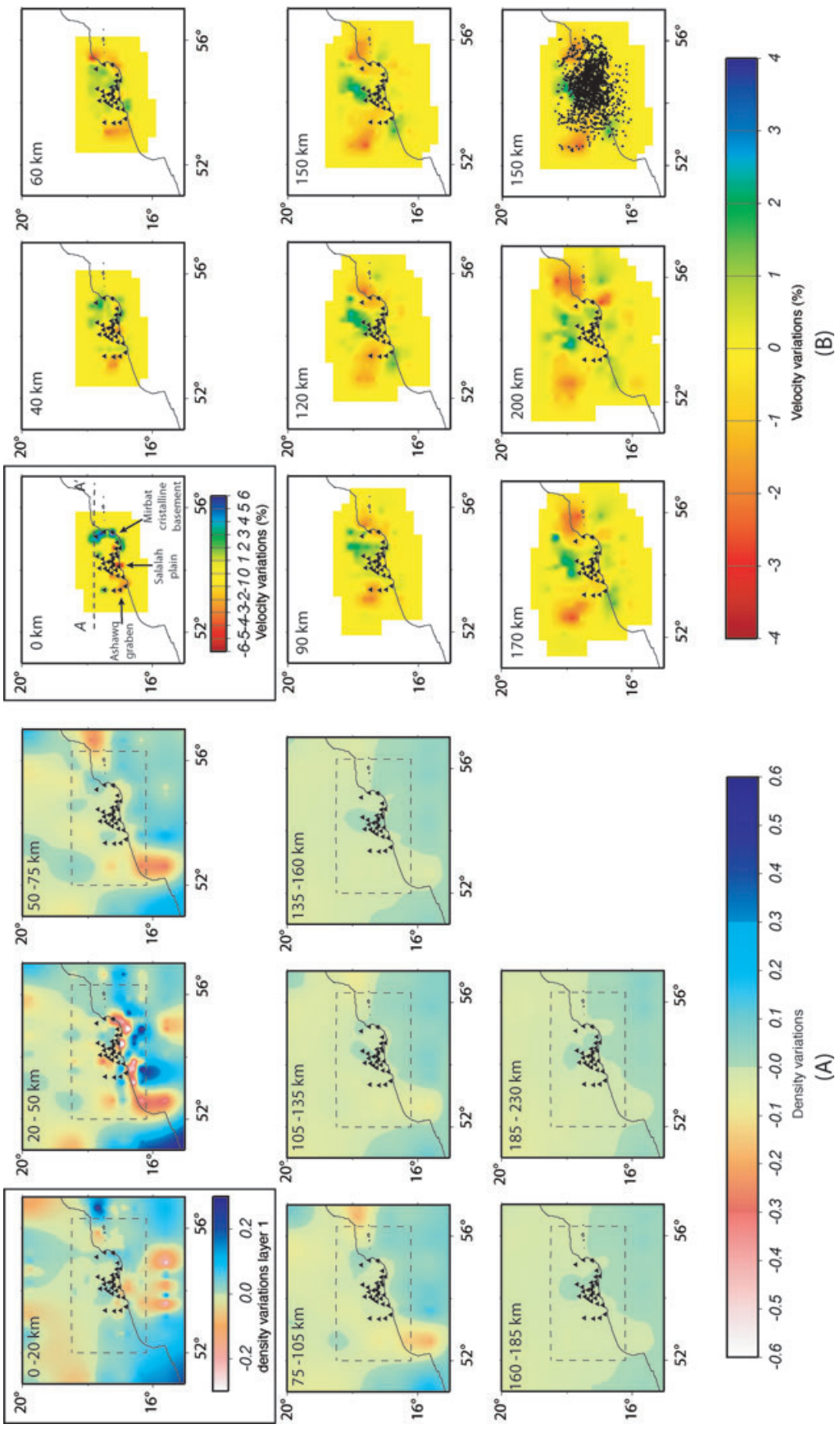

Figure 5. Evolution of the root mean square through the iterations for delay times (top panel) and gravity anomalies (bottom panel).

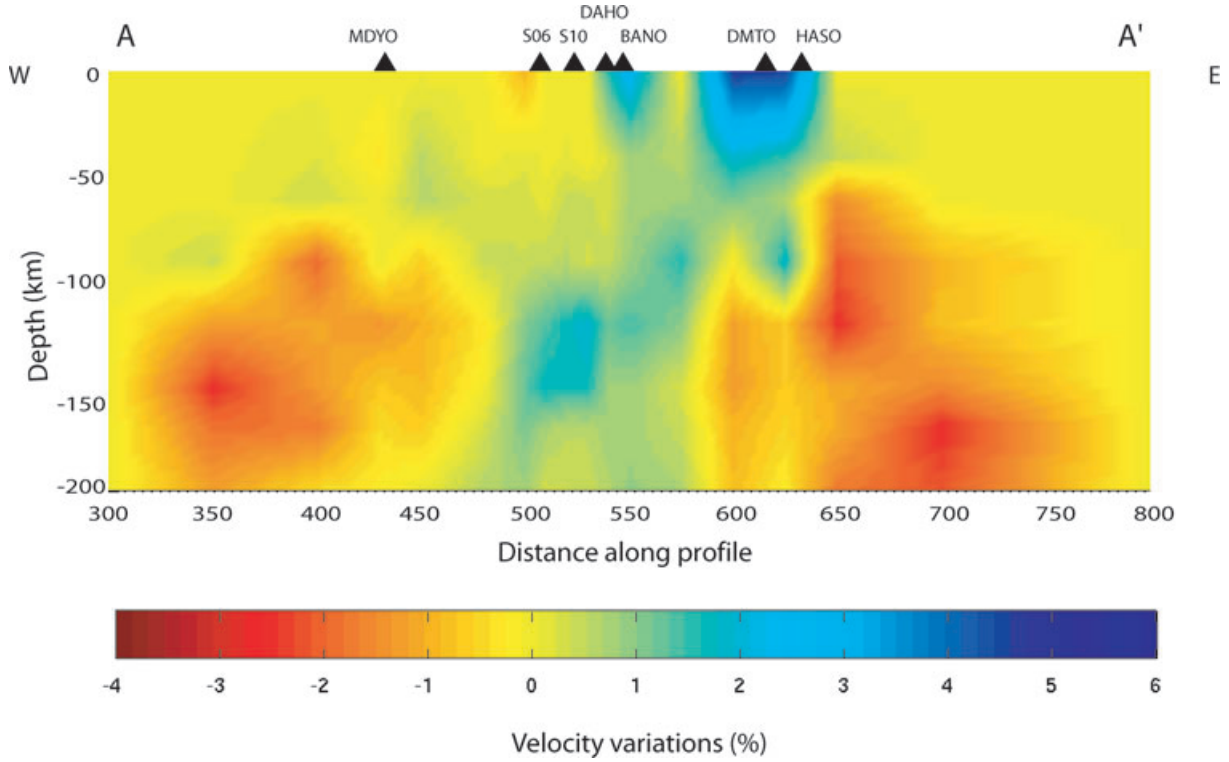

Figure 6. Final density (a) and *P*-wave velocity (b) models obtained from joint inversion. Seismic stations are located with the black triangles. (a) The dashed box indicates the region of gravity data used in the inversion. (b) The dashed line in the first layer shows the AA′ profile along which the cross-section of Fig. 7 is made. The last slice of the velocity model shows the piercing points of rays at 150 km depth. Note the colour bar change between the first layer and the other slices of the models.

We suggest two main reasons to explain this apparent inconsistency for layer 2. The first one is the gravity edge effect on passive margins that comes from the superimposition of several signals and sources (as illustrated in Fig. 8) (e.g. Worzel 1968; Watts & Stewart 1998): (1) the juxtaposition of thick, low-density continental crust with thin, high-density oceanic crust; (2) the presence of sediment-filled rifted basins and (3) the Moho depth variations. In our case, the sum of those signals results in a global gravity signature from which we can hardly isolate one of the sources. It thus increases our difficulties to understand the margin structures. However, our results delineate the horizontal extent of the basins, where additional *a priori* information will be necessary to completely overcome this problem.

The second reason we advocate here is that the incident angle of the teleseismic rays used for the joint inversion is small enough to prevent any ray crossings within the uppermost 10–15 km (e.g. Evans & Achauer 1993). As the seismic analysis is at the edge of its resolution, we cannot benefit from the complementarity of the data sets here to overcome this gravity edge effect (Fig. 8). A more detailed analysis of the short wavelength gravity anomalies should be proceeded to better investigate the crustal structure of the Dhofar margin. However, to completely overcome the gravity edge effect near the passive margin, additional constraints are needed from both receiver functions for all stations and seismic profiles obtained during the Encens cruise (Leroy *et al.* 2009b). This work is in progress, but clearly beyond the scope of this study.

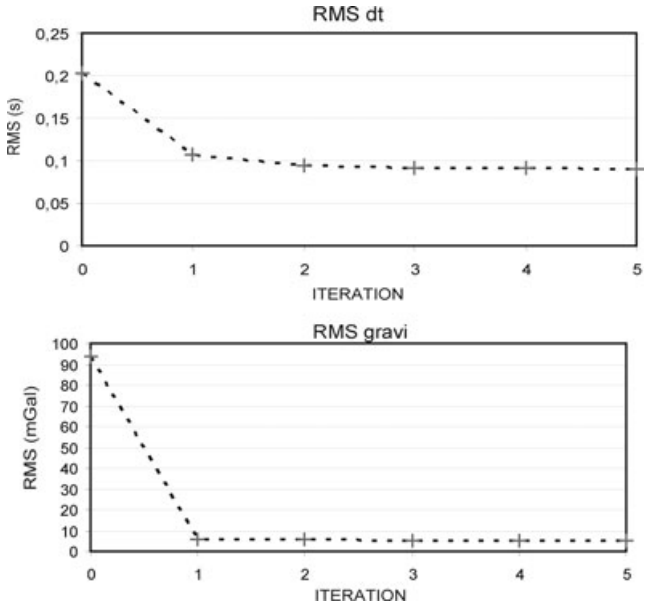

Figure 7. Cross-section along the west–east profile AA′ (see Fig. 6 the location and orientation of AA′) through the final *P*-wave velocity model obtained by joint inversion. The nearest seismic stations (black triangles) are projected along AA′.

4.3 Upper mantle structure

The upper mantle structure is imaged by layers 3 (at 50 km) down to 8 (230 km). The resulting anomalies vary between ±0.3 g cm^{-3} and ±4 per cent for the density and velocity, respectively. The density model exhibits a long wavelength pattern constant through all the mantle layers: the onshore part of the margin appears less dense than the offshore part (Fig. 6). We interpret this to be the transition from

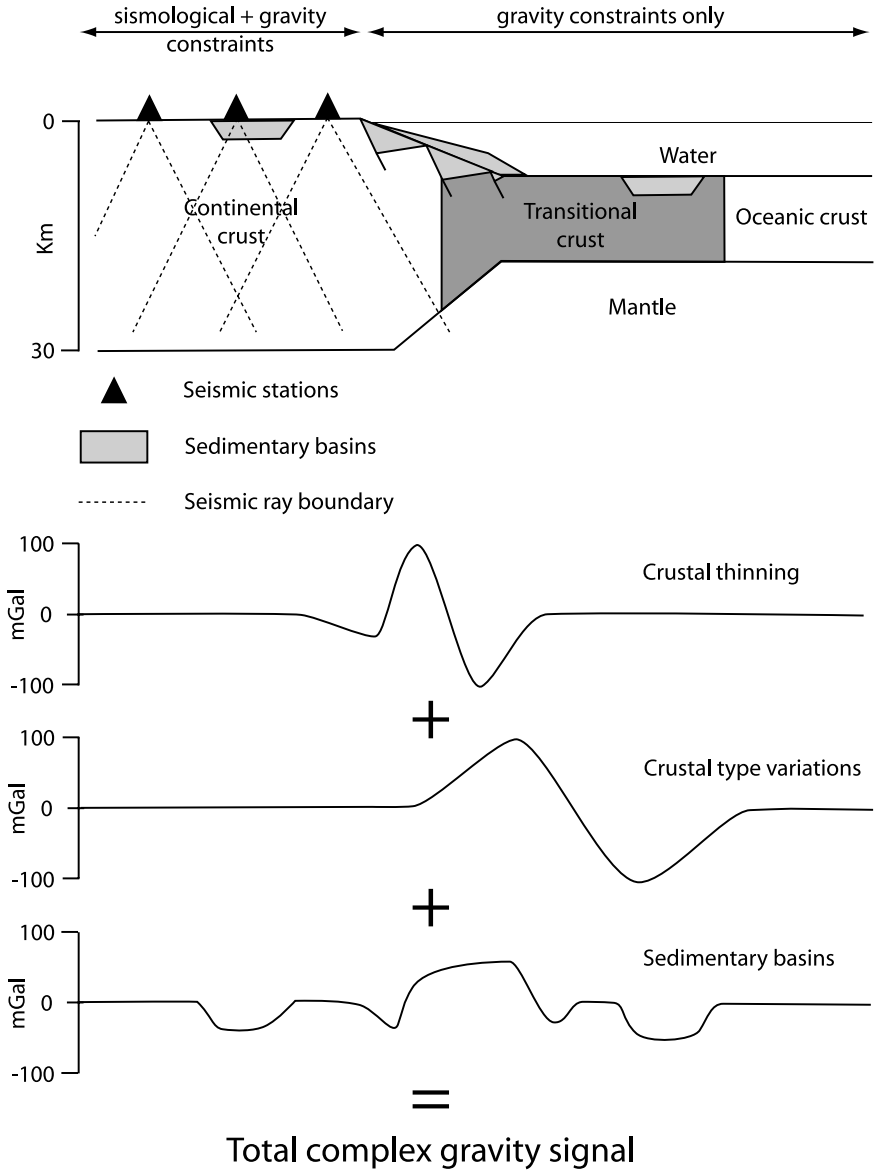

Figure 8. Scheme of the gravity edge effect at a continental passive margin. The total gravity anomaly is the sum of various effects: crustal thinning, the presence of a transitional crust, sedimentary basins. The presence of underplating and/or crustal and mantle bodies with density variations can result in an even more complex gravity signal. In our case, because of seismic ray coverage, the offshore crustal part is constrained by gravity only.

continental to oceanic crust and mantle. This pattern is not seen in velocity because the upper oceanic part is certainly not sampled by the rays due to the geometry of the teleseismic raypath (Evans & Achauer 1993) (Fig. 8).

In more detail, our inversion reveals two intriguing patterns in its deepest part where two negative anomalies appear at both sides of the network. For the density model, they start at 50 km, then slightly decrease in amplitude until 230 km. These anomalies are more pronounced and obvious in the velocity model where they display -3 per cent of amplitude from 60 to 230 km depth. In between them is a positive anomaly ($\approx +2$ per cent and $+0.1$ g cm^{-3} in velocity and density, respectively) centred on the network. The width of these anomalies is approximately 100 km.

The density model exhibits the same pattern, even though the amplitudes of the anomalies are weak due to the decay of signal with distance (Fig. 6).

Determining the cause and the reality of these anomalies is not self-evident. First, as the velocity and density contrasts show a zero average for a given layer, we are unable to distinguish between two strong negative anomalies (the positive one being an artifact) or one central big positive one (the negative ones being an artefact). Secondly, determining the cause of seismic heterogeneity within the Earth is always problematic because a number of factors (such as temperature, compositional variations, presence of melt or water, anisotropy) can play a role in wave speed variations in tomographic models (e.g. Karato 1993; Sobolev *et al.* 1996). Furthermore, those factors do not affect wave propagation the same way. As an example, temperature is thought to influence wave velocity more than compositional variations (see overviews of Ranalli 1996; Yuen *et al.* 1996). Moreover, temperature has the same effect on *P*- than on *S*-wave velocity, contrary to the effects of rock composition, the presence of a fluid phase and an elasticity (e.g. Karato 1993).

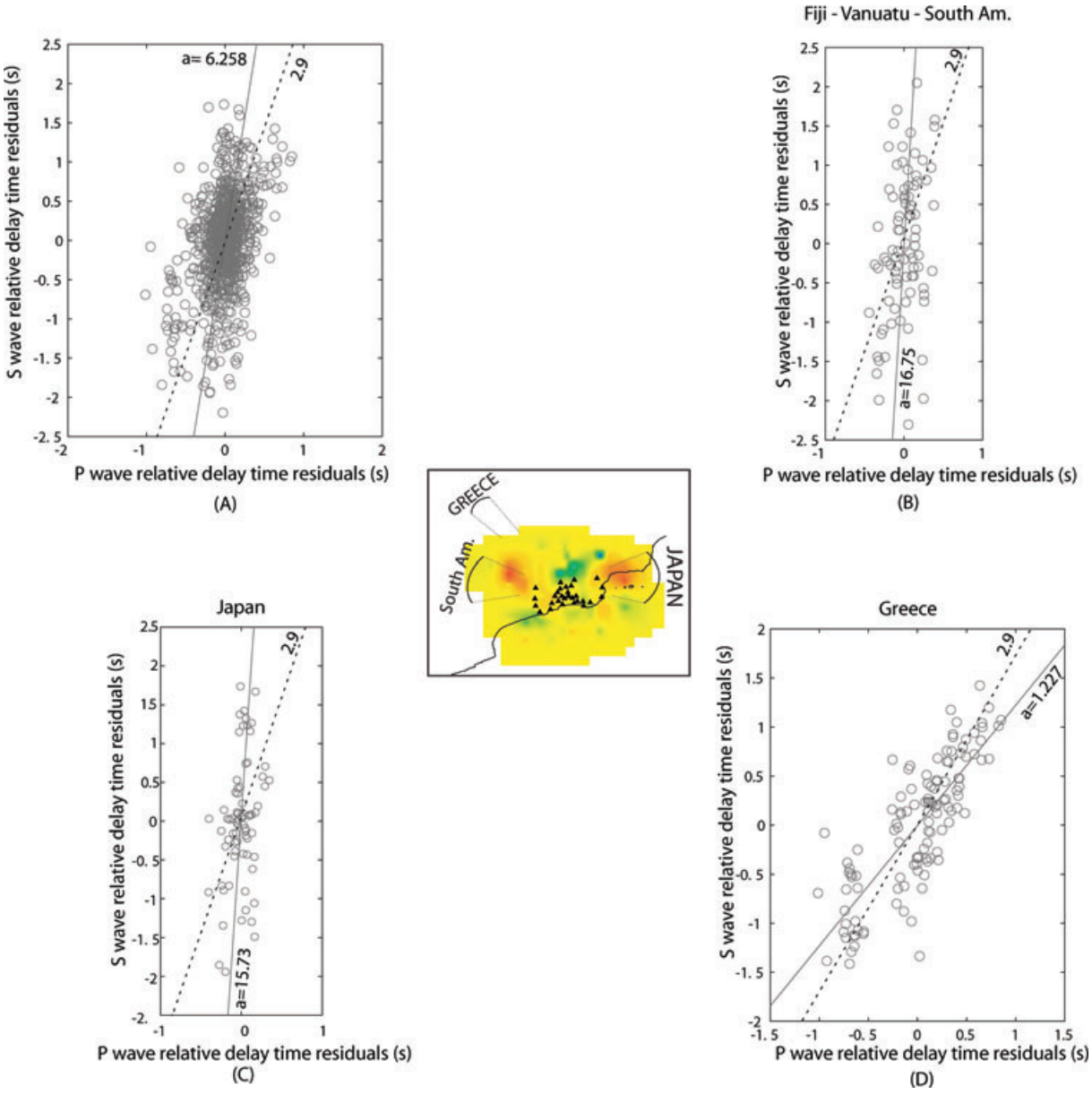

Figure 9. Plots of *P*-wave versus S-wave relative arrival time residuals for all stations and common earthquakes. (a) All events are considered, (b) only events passing through the eastern negative anomaly (from Fiji, Vanuatu and South America), (c) only events passing through the western negative anomaly (from Japan) and (d) events passing through the positive one (from Greece). The solid lines are the least square fit to our data (with a the slope of the lines), and the dashed one is a slope of 2.9 (thermal effect only). The central part shows the direction of the rays coming from South America, Greece and Japan.

However, compositional effects are generally considered secondary to temperature (e.g. Goes *et al.* 2000; Cammarano *et al.* 2003; Faul & Jackson 2005; Bastow *et al.* 2008). To determine within the possible sets of causes for these deep anomalies, we plot *S* versus *P* traveltime residuals, following the manner of Gao *et al.* (2004) or Bastow *et al.* (2005). Such a comparison is preferable to directly analyze the velocity anomalies on our tomographic images because it requires fewer assumptions, particularly associated with amplitude recovery. Indeed, using the range of temperature derivatives of Bastow *et al.* (2005) ($\delta V_P = 0.5$–2 per cent per 100°) on our results, we obtain temperatures for the anomalies that spread over a unreasonably large range (100° and 1200°) to confirm or refute possible partial melting. Fig. 9 shows plots of *P* versus *S* traveltime residuals for common earthquakes at all stations. Based on Karato (1993) and for a purely thermal origin, Gao *et al.* (2004) determined a linear relationship with a slope of 2.9 between *P* and *S* traveltime residuals. Considering all events, we find a slope greater than 2.9, suggesting the presence of partial melt (Bastow *et al.* 2005) (Fig. 9a). To determine whether the two negative velocity anomalies are associated with the occurence of partial melting, we plot *P* versus *S* residuals for rays that pass through the anomalies (Figs 9b and c). The slopes are then even steeper. Finally, the slope for rays not passing through the two negative velocity anomalies is less than 2.9 (Fig. 9d). It is thus likely that the zones of the two negative velocity anomalies are real and the location of partial melt.

Some studies investigated the effect of melt geometry on seismic velocities (e.g. Mavko 1980). For a given melt fraction crack-like pore space has a more dramatic effect on velocity than

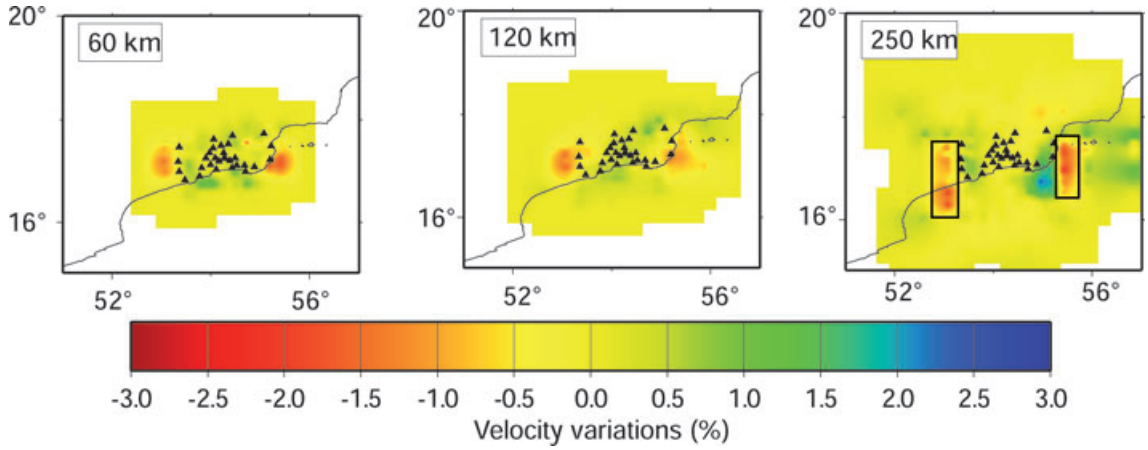

Figure 10. Synthetic spike test for the joint inversion of gravity and seismological data. Depth slices into the retrieved velocity model. The two rectangles show the location of the input density (-0.16 g cm^{-3}) and velocity (-5 per cent) contrasts placed between 230 and 280 km.

equi-dimensionsal pore space. Thus, Saltzer & Humphreys (1997) use the following relationship:

$$\frac{\Delta V_{\mathrm{P}}}{V_{\mathrm{P}}} = A\Phi,$$

where Φ is the melt fraction and A is a constant dependent upon the aspect ratio of the melt inclusions. Generally, $1 < A < 3$ unless the melt is distributed in very thin films, in which case A may be larger. In our study, the smearing effect and the smoothing constraint of our inversion do not allow us to accurately define $\frac{\Delta V_{\mathrm{P}}}{V_{\mathrm{P}}}$. But the synthetic tests have shown that we can retrieve half the amplitude of the velocity anomalies. With a maximum $\frac{\Delta V_{\mathrm{P}}}{V_{\mathrm{P}}}$ of about 3 per cent observed on our results, the real amplitude could then be as much as 6 per cent further implying a melt fraction of about 2–6 per cent.

5 RESOLUTION OF SPIKE ANOMALIES

To investigate the resolving power of our inversion for the deepest parts of the models, which are also the hardest to image, we perform a spike test. In this test, we added an extra layer between 230 and 280 km for density blocks and at 250 km depth for velocity nodes. Inside this last layer, we inserted two negative anomalies on both sides of the seismic network. We set their velocity and density contrasts to -5 per cent and -0.16 g cm^{-3}, respectively (Fig. 10). We chose negative anomalies because the seismic rays tend to avoid the regions of low velocity, and hence these are the hardest to retrieve in tomography.

Fig. 10 shows the results of our synthetic spike velocity model. The anomalies are quite well retrieved, yet with an obvious vertical smearing effect as the negative values are recovered from about 60 to 250 km depth. The positive velocity anomaly located between the negative anomalies is an artefact due to the fact that the inversion deals with relative anomalies, and that the average should be zero within the layer (Zeyen & Achauer 1997). Concerning the density model, the inversion is able to only retrieve a weak part of the anomalies at the real depth. The highest density contrasts are retrieved for the 60 km layer, due to the smearing effect.

Even if there are inherent effects in our inversion, these tests clearly illustrate the complementarity of the two data sets. The crustal part is better resolved by the gravity constraints, whereas the deeper parts are resolved by the seismic constraints: the larger the number of crossing rays, the better the resolution.

6 DISCUSSION

We have investigated the crustal and mantle structure along the northern rifted margin of the Gulf of Aden with gravity and seismological data. In the following section, we discuss our results in terms of geological and geodynamical processes.

The very upper part of our models (upper crust, 0–20 km) displays anomalies directly related to major geological units observed at the surface. The Salalah and Ashawq grabens with sedimentary infill are characterized by negative anomalies both in velocity and density, whereas Precambrian basement outcrops at the eastern end of the network in the Mirbat area with high density and velocity signatures (Fig. 6). The lower crustal part of our models (20–50 km) is the location of an apparent decoupling between velocity and density information. We explain this behaviour by the gravity edge effect well-known on rifted passive margins, and by the fact that seismic rays do not have sufficient coverage at that particular depth to resolve the sharp lateral heterogeneity. To tackle this question, we propose to invert the short to average wavelengths of the gravity signal with constraints from receiver functions and multichannel seismic profiles available in the region (Encens cruise). First, this will lead to a better resolution of the area. Secondly, we expect to overstep the gravity edge effect and dissociate the different sources of the signal with a finer parametrization. However, this work is beyond the scope of the present study and will be soon undertaken.

The deep part of the gravity and velocity models is dominated by two negatives anomalies (Fig. 6). These two regions are probably the location of partial melting within the mantle. We crudely estimate the amount of partial melting to be between 2 and 6 per cent from the amplitude of our anomalies.

To assist the discussion, we project our velocity results for 170 km depth (layer 7) on the regional tectonic scheme (d'Acremont *et al.* 2006, Fig. 11). As shown with the checkerboard test, our results present a fairly good lateral velocity resolution for this depth even for regions outside the seismic array, as the ray crossing widens with depth (see also Fig. 6b).

The vertical extent of these negative anomalies is yet not well constrained because of the smearing effect. However, there are no strong negative density variations in the shallowest layers of the final model at the location of the two velocity perturbations (Fig. 6). This distribution testifies for deep anomalies. Besides, we have estimated

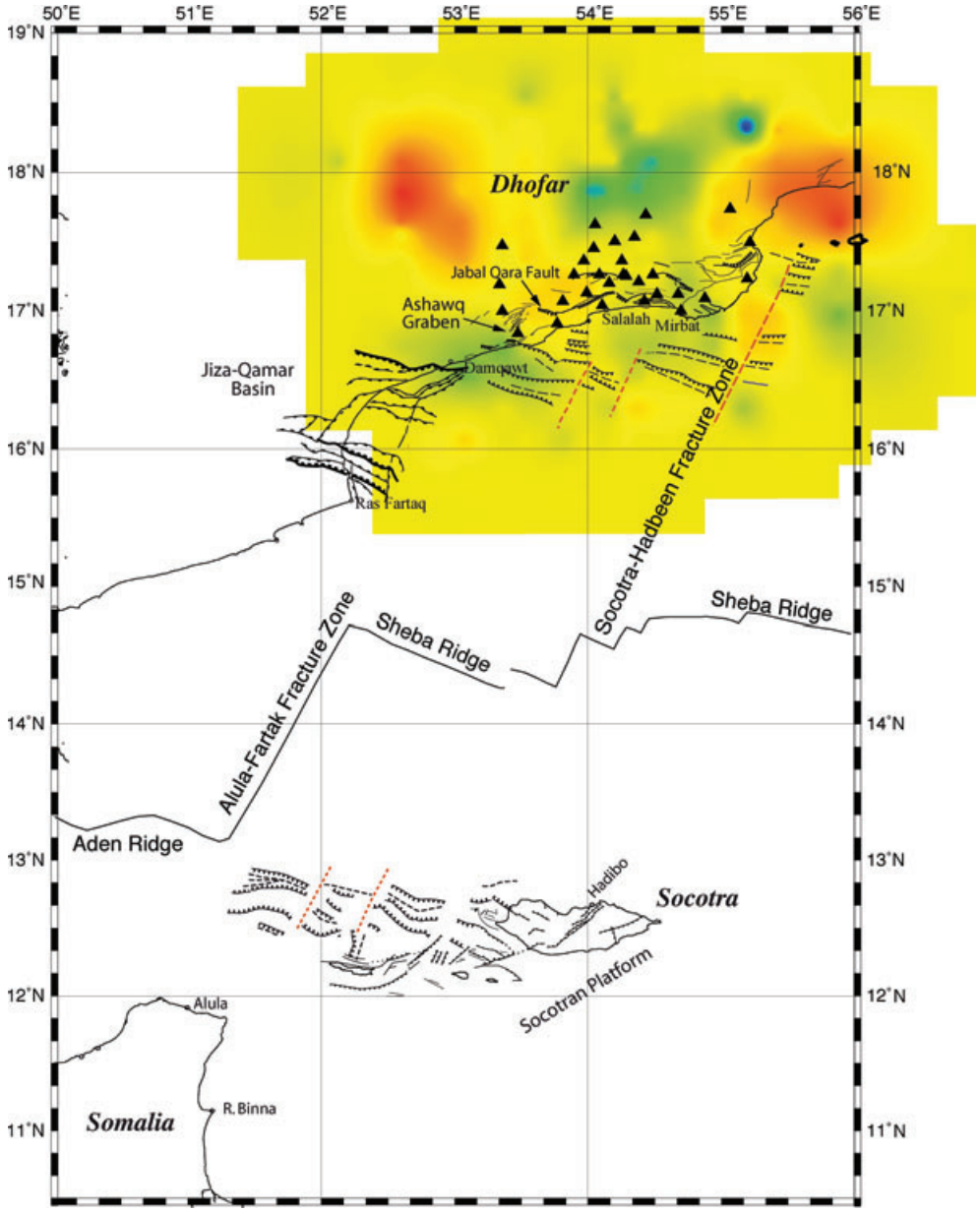

Figure 11. *P*-wave velocity perturbation model at 170 km depth above the tectonic scheme from d'Acremont (2002). Main faults are underlined by black segments, and brown dashed lines offshore indicate major segmentation of the northern Aden margin (from d'Acremont *et al.* 2005).

that 60 km is a reasonable depth for still having seismic smearing effect from a single perturbing body located even below 200 km depth (see synthetic spike test; Fig. 10). We then are totally aware that the low-velocity zones may be deeper than it seems from Fig. 6, may be below 80–100 km depth. The only way to constrain their extension in depth is then to discuss their existence from previous tomography studies imaging the deeper part of the mantle. Even if no other lithospheric tomography is available in the whole Gulf of Aden, it is quite interesting to notice that a minimum of surface wave phase velocity is also imaged in the eastern part of the Gulf in the recent studies of Sebai *et al.* (2006) and the one of Pasyanos & Nyblade (2007). In these models, a low-velocity area is located between Socotra-Hadbeen and Alula-Fartak fracture zones at about 100 km depth, and not below 200 km. We estimate then that these low velocity zones do not exceed ≈200 km and are restricted to the upper mantle.

The striking pattern of these two anomalies is that they are exactly located on the prolongation of the two fracture zones of Socotra-Hadbeen and Alula-Fartak (Fig. 11). We are thus very tempted to relate their presence with the rifting process and the margin evolution and their segmentation (d'Acremont *et al.* 2006). However, the lateral extension of our network is too limited (max. 400 km) to fully interpret our results in light of more regional geodynamic processes (Afar plume, Sheba ridge). Particularly, no direct connection between our anomalies and the Sheba ridge is evidenced in our study. Moreover, the joint inversion only gives an image for the present anomalous structures. We thus do not have the slightest indication of the age of these low velocity zones relative to the rifting process (pre- syn- or post-rift). They are too deeply rooted to perturb the heat flow, which exhibits normal values for a continental lithosphere (40–47 mW m^{-2}; Lucazeau *et al.* 2008).

Evidence has been brought for mantle melt migration controlled by lithospheric thickness variations (e.g. Ebinger & Sleep 1998; Manglik & Christensen 2006). Ridges with large offset transform faults are also conducive to lateral melt migration. Escartin & Cannat (1999) explain a discrepancy in crustal thickness deduced from geophysical and geological studies by along-axis melt migration away from the transform (Mid-Atlantic Ridge). Interactions between plume and ridge have also been reported near the Galapagos area (Ito *et al.* 1997). In this case, lateral mantle flow of melt is proposed to explain plume-signature material nearby mid-ocean ridges (Braun & Sohn 2003). In favourable conditions (temperature and migration velocity), the melt can cross offsets of several hundred kilometers in a few hundreds thousand years (Braun & Sohn 2003).

Although no direct evidence has been reported of melt migration between the Sheba ridge and the fracture zones of Socotra-Hadbeen and Alula-Fartak, such a mechanism could associate the low-velocity zones we have evidenced with the Sheba ridge. With no more indications on the age of these anomalous zones, we then propose the following two options:

(1) The melting zones are pre- or syn-rift and then favoured the location of the ridge segmentation (Socotra-Hadbeen and Alula-Fartak FZ), regardless of inherited structures (e.g. Jiza-Qamar Basin Mesozoic in age and Proterozoic basement; Fig. 11);

(2) The melting zones are post-rift and come from the migration of melt from the Sheba ridge along the Alula-Fartak and Socotra-Hadbeen FZ. This alternative is consistent with the presence of recent thermal episodes recorded in the Sheba ridge axis and off-axis (from immediately after the break-up up to now) in between the Alula-Fartak and Socotra-Hadbeen fracture zones that are best explained by channeled flow of plume material from Afar along the Aden-Sheba ridges (Leroy *et al.* 2009a). Heat flow measurements and multichannel seismic observations indicative of recent volcanic activity (Lucazeau *et al.* 2009; Autin *et al.* 2009) along the deep part of this margin are consistent with this inference.

7 CONCLUSIONS

We performed a joint inversion for gravity and teleseismic data to image lithospheric structure beneath the northeast non-volcanic passive margin of the Gulf of Aden. The crustal part of the model is dominated by rifted basins with sedimentary infill, the change between oceanic and continental crustal composition together with crustal thickness variations. Deep anomalies within the mantle are coherently imaged by both the seismic and gravity signals. We infer two zones of partial melting (max. 6 per cent) in the direction of the main fracture zones (Alula-Fartak and Socotra-Hadbeen). The presence of these partial melting zones questions the non-volcanic style of this margin, together with their sources (Sheba ridge) and timing (pre-, syn-, post-rift). This inversion of gravity and teleseismic data only images the present day state of lithospheric heterogeneity. We have no evidence about timing of the development of such structures and need other studies to further our interpretations (SKS studies, deep receiver functions).

ACKNOWLEDGMENTS

The authors express their deep thanks to Dr H. Al-Azri, S. Al-Busaıdi, S. Bin Monsheer Balahaf from the Directory of Minerals of Oman, for their help on the field and for administration assistance. The authors also thank Dr I. El Hussein from the Sultan Qaboos University (Earthquake Monitoring Center), for his welcoming assistance. The Seismic Dhofar Experiment was funded by GDRMarges in 2003–2004 and by NERC for 2005–2006 (NE/C514031/1). We acknowledge the Geophysical Equipment Facility (NERC) for the loan of seismic stations we deployed in Sultanate of Oman, for the two networks. All the people who helped during the deployment and servicing are here greatly thanked (E. d'Acremont, D. Keir, C. Brunet, C. Petit, L. Labrousse, V. Famin).

REFERENCES

Al-Damegh, K., Sandvol, E., Al-Lazki, A. & Barazangi, M., 2004. Regional seismic wave propagation (Lg and Sn) and Pn attenuation in the Arabian Plate and surrounding regions, *Geophys. J. Int.,* **157**(2), 775–795.

Al-Damegh, K., Sandvol, E. & Barazangi, M., 2005. Crustal structure of the Arabian plate; New constraints from the analysis of teleseismic receiver functions, *Earth planet. Sci. Lett.,* **231,** 177–196.

Al-Lazki, A., Sandvol, E., Seber, D., Barazangi, M., Turkelli, N. & Mohamad, R., 2004. Pn tomographic imaging of mantle lid velocity and anisotropy at the junction of the Arabian, Eurasian and African plates, *Geophys. J. Int.,* **158**(3), 1024–1040.

Al-Lazki, A.I., Seber, D., Sandvol, E. & Barazangi, M., 2002. A crustal transect across the Oman Mountains on the eastern margin of Arabia, *GeoArabia,* **7,** 47–78.

Audin, L. *et al.,* 2004. Paleomagnetism and K-Ar and 40AR/39Ar ages in the Ali Sabieh area (Republic of Djibouti and Ethiopia): constraints on the mechanism of Aden ridge propagation into southeastern Afar during the last 10 Myr, *Geophys. J. Int.,* **158,** 327–345.

Autin, J. *et al.,* 2009. Continental break-up history of a deep magma-poor margin from seismic reflection data (northeastern Gulf of Aden margin, offshore Oman, *Geophys. J. Int.*, in press, doi:10.1111/j.1365-246X.2009.04424.x (this issue).

Bastow, I., Stuart, G., Kendall, J.-M. & Ebinger, C., 2005. Upper-mantle seismic structure in a region of incipient continental break-up: northern Ethiopian rift, *Geophys. J. Int.,* **162,** 479–493.

Bastow, I., Nyblade, A., Stuart, G., Rooney, T. & Benoit, M., 2008. Upper mantle seismic structure beneath the Ethiopian hot spot: rifting at the edge of the African low-velocity anomaly, *Geochemistry Geophysics Geosystems,* **9**(12), Q12022.

Bellahsen, N., Faccenna, C., Funiciello, F., Daniel, J.M. & Jolivet, L., 2003. Why did Arabia separate from Africa? Insights from 3-D laboratory experiments, *Earth planet. Sci. Lett.,* **216,** 365–381.

Bellahsen, N., Fournier, M., d'Acremont, E., Leroy, S. & Daniel, J.-M., 2006. Fault reactivation and rift localization: the northeastern Gulf of Aden margin., *Tectonics,* **25,** TC1007.

Benoit, M.H., Nyblade, A.A., VanDecar, J.C. & Gurrola, H., 2003. Upper mantle P wave velocity structure and transition zone thickness beneath the Arabian Shield, *Geophys. Res. Lett.,* **30,** 1531.

Birch, F., 1961. The velocity of compressional waves in rocks to 10 kilobars, 2, *J. geophys. Res.,* **66,** 2199–2224.

Blakely, R., 1995. *Potential Theory in Gravity and Magnetic Applications,* Cambridge University Press, New York.

Braun, M.G. & Sohn, R.A., 2003. Melt migration in plume-ridge systems, *Earth planet. Sci. Lett.,* **213,** 417–430.

Buck, W., 2004. Consequences of asthenospheric variability on continental rifting, *Rheol. Deformat. Lithos. Continental Margins,* pp. 1–30.

Cammarano, F., Goes, S., Vacher, P. & Giardini, D., 2003. Inferring upper-mantle temperatures from seismic velocities, *Phys. Earth planet. Int.,* **138**(3-4), 197–222.

Christensen, N.I. & Mooney, W.D., 1995. Seismic velocity structure and composition of the continental crust: a global view, *J. geophys. Res.,* **100,** 9761–9785.

Courtillot, V., Jaupart, C., Manighetti, I., Tapponnier, P. & Besse, J., 1999. On causal links between flood basalts and continental breakup, *Earth planet. Sci. Lett.,* **166,** 177–195.

Debayle, E., Lévèque, J.-J. & Cara, M., 2001. Seismic evidence for a deeply rooted low-velocity anomaly in the upper mantle beneath the northeastern Afro/Arabian continent, *Earth planet. Sci. Lett.,* **193,** 423–436.

d'Acremont, E., 2002. De la déchirure continentale à l'accrétion océanique: ouverture du golfe d'Aden, *PhD thesis*, Université de Paris VI.

d'Acremont, E., Leroy, S., Beslier, M.-O., Bellahsen, N., Fournier, M., Robin, C., Maia, M. & Gente, P., 2005. Structure and evolution of the eastern Gulf of Aden conjugate margins from seismic reflection data, *Geophys. J. Int.,* **160,** 869–890.

d'Acremont, E., Leroy, S., Maia, M., Patriat, P., Beslier, M.-O., Bellahsen, N., Fournier, M. & Gente, P., 2006. Structure and evolution of the eastern Gulf of Aden: insights from magnetic and gravity data (Encens-Sheba, MD117 cruise), *Geophys. J. Int.,* **185,** 786–804.

Ebinger, C. & Sleep, N., 1998. Cenozoic magmatism throughout East Africa resulting from impact of a single plume, *Nature,* **395,** 788–791.

Escartin, J. & Cannat, M., 1999. Ultramafic exposures and the gravity signature of the lithosphere near the Fifteen-Twenty Fracture Zone (Mid-Atlantic Ridge, 14°-16.5°N), *Earth planet. Sci. Lett.,* **171,** 411–424.

Evans, J. & Achauer, U., 1993. Teleseismic velocity tomography using the ACH method: theory and application to continental scale, in *Seismic Tomography Theory and Practice,* pp. 319–360, Chapman and Hall, London.

Faul, U.H. & Jackson, I., 2005. The seismological signature of temperature and grain size variations in the upper mantle, *Earth planet. Sci. Lett.,* **234,** 119–134.

Fournier, M., Patriat, P. & Leroy, S., 2001. Reappraisal of the Arabia-India-Somalia triple junction kinematics, *Earth planet. Sci. Lett.,* **189,** 103–114.

Gao, W., Grand, S., Baldridge, W., Wilson, D., West, M., Ni, J. & Aster, R., 2004. Upper mantle convection beneath the central Rio Grande rift imaged by P and S wave tomography, *J. geophys. Res.,* **109**, B03305, doi:10.1029/2003JB002743.

Goes, S., Govers, R. & Vacher, P., 2000. Shallow mantle temperatures under Europe from P and S wave tomography, *J. geophys. Res.,* **105**(B5), 11153–11169.

Hansen, S., Schwartz, S., Al-Amri, A. & Rodgers, A., 2006. Combined plate motion and density-driven flow in the asthenosphere beneath Saudi Arabia: evidence from shear-wave splitting and seismic anisotropy, *Geology,* **34,** 869–872.

Hébert, H., Deplus, C., Khanbari, K. & Audin, L., 2001. Lithospheric structure of a nascent spreading ridge inferred from gravity data: the western Gulf of Aden, *J. geophys. Res.,* **106,** 26 345–26 363.

Huchon, P. & Khanbari, K., 2003. Rotation of the syn-rift stress field of the northern Gulf of Aden margin, Yemen, *Tectonophysics,* **364,** 147–166.

Ito, G., Lin, J. & Gable, C.W., 1997. Interaction of mantle plumes and migrating mid-ocean ridges: implications for the Galapagos plume-ridge system, *J. geophys. Res.,* **102,** 15 403–15 417.

Jordan, M. & Achauer, U., 1999. A new method for the 3-D joint inversion of teleseismic delaytimes and Bouguer gravity data with application to the French Massif Central, *EOS Trans. AGU, Fall Meet. Suppl.,* **80(46)**(S31A-08).

Karato, S., 1993. Importance of anelasticity in the interpretation of seismic tomography, *Geophy. Res. Lett.,* **20,** 1623–1626.

Kennett, B. & Engdahl, E., 1991. Traveltimes for global earthquake location and phase identification, *Geophys. J. Int.,* **105,** 429–465.

Knox, R.P., Nyblade, A.A. & Langston, C.A., 1998. Upper mantle S velocities beneath Afar and western Saudi Arabia from Rayleigh wave dispersion, *Geophy. Res. Lett.,* **25,** 4233–4236.

Lees, J. & VanDecar, J., 1991. Seismic tomography constrained by Bouguer gravity anomalies: Applications in western Washington, *Pure appl. Geophys.,* **135,** 31–52.

Lepvrier, C., Fournier, M., Bérard, T. & Roger, J., 2002. Cenozoic extension in coastal Dhofar (southern Oman): implications on the oblique rifting of the Gulf of Aden, *Tectonophysics,* **357,** 279–293.

Leroy, S. *et al.,* 2004. From rifting to spreading in the eastern Gulf of Aden: a geophysical survey of a young oceanic basin from margin to margin, *Terra Nova,* **16,** 185–192.

Leroy, S. *et al.,* 2006. The onshore-offshore encens project: imaging the stretching of the continental lithosphere and inception of oceanic spreading in the eastern Gulf of Aden, *AGU Fall Meeting Abstracts,* **87(52)**(T53A-1567), 1567.

Leroy, S., d'Acremont, E., Tiberi, C., Basuyau, C., Autin, J. & Lucazeau, F., 2009a. Recent off-axis volcanism in the eastern Gulf of Aden: implications for plume-ridge interactions, *Earth planet. Sci. Lett.*, submitted.

Leroy, S. *et al.,* 2009b. Contrasted styles of rifting in the eastern Gulf of Aden, *EOS Trans. AGU Fall Meet. Suppl.,* T31C-1838.

Lines, L., Schultz, A. & Treitel, S., 1988. Cooperative inversion of geophysical data, *Geophysics,* **53,** 8–20.

Lizarralde, D. *et al.,* 2007. Variation in styles or rifting in the Gulf of California, *Nature,* **448,** 466–469.

Lucazeau, F. et al., 2008. Persistent thermal activity at the Eastern Gulf of Aden after continental break-up, *Nature Geoscience,* **1,** 854–858.

Lucazeau, F. et al., 2009. Post rift Volcanism and high heat-flow at the Ocean-Continent transition of the Gulf of Aden, *Terra Nova*, **21**(4), 285–292.

Manglik, A. & Christensen, U.R., 2006. Effect of lithospheric root on decompression melting in plume-lithosphere interaction models, *Geophys. J. Int.,* **164,** 259–270.

Manighetti, I., Tapponnier, P., Courtillot, V., Gruszow, S. & Gillot, P., 1997. Propagation of rifting along the Arabia-Somalia plate boundary: the Gulfs of Aden and Tadjoura, *J. geophys. Res.,* **102,** 2681–2710.

Mavko, G.M., 1980. Velocity and attenuation in partially molten rocks, *J. geophys. Res.,* **85,** 5173–5189.

Park, Y., Nyblade, A.A., Rodgers, A.J. & Al-Amri, A., 2007. Upper mantle structure beneath the Arabian Peninsula and northern Red Sea from teleseismic body wave tomography: implications for the origin of Cenozoic uplift and volcanism in the Arabian Shield, *Geochemistry, Geophysics, Geosystems,* **8,** Q06021, doi:10.1029/2006GC001566.

Pasyanos, M.E. & Nyblade, A.A., 2007. A top to bottom lithospheric study of Africa and Arabia, *Tectonophysics,* **444,** 27–44.

Ranalli, G., 1996. Seismic tomography and minerals physics, in *Seismic modelling of Earth structure,* pp. 443–461, ed. Editrice Compositori, Bologna.

Roger, J., Platel, J., Cavelier, C. & Grisac, C., 1989. Données nouvelles sur la stratigraphie et l'histoire géologique du Dhofar, *Bull. Soc. Géol. France,* **5,** 265–277.

Saltzer, R.L. & Humphreys, E.D., 1997. Upper mantle *P* wave velocity structure of the eastern Snake River Plain and its relationship to geodynamic models of the region, *J. geophys. Res.,* **102,** 11 829–11 842.

Sebai, A., Stutzmann, E., Montagner, J.-P., Sicilia, D. & Beucler, E., 2006. Anisotropic structure of the African upper mantle from Rayleigh and Love wave tomography, *Phys. Earth planet. Int.,* **155,** 48–62.

Sobolev, S.V., Zeyen, H., Stoll, G., Werling, F., Altherr, R. & Fuchs, K., 1996. Upper mantle temperatures from teleseismic tomography of French Massif Central including effects of composition, mineral reactions, anharmonicity, anelasticity and partial melt, *Earth planet. Sci. Lett.,* **139,** 147–163.

Tard, F., Masse, P., Walgenwitz, F. & Gruneisen, P., 1991. The volcanic passive margin in the vicinity of Aden, Yemen, *Bul. Centr. Rech. Explor. Prod.,* **15,** 1–9.

Thurber, C.H., 1983. Earthquake locations and three-dimensional crustal structure in the Coyote Lake area, Central California, *J. geophys. Res.,* **88,** 8226–8236.

Tiberi, C., Diament, M., Déverchère, J., Mikhailov, V., Tikhotsky, S. & Achauer, U., 2003. Deep structure of the Baikal rift zone revealed by joint inversion of gravity and seismology, *J. geophys. Res.,* **108,** 2133.

Tiberi, C., Leroy, S., d'Acremont, E., Bellahsen, N., Ebinger, C., Al-Lazki, A. & Pointu, A., 2007. Crustal geomotry of the northeastern Gulf of Aden passive margin: localization of the deformation inferred from receiver function analysis, *Geophys. J. Int.,* **168,** 1247–1260.

Ukstins, I., Renne, P., Wolfenden, E., Baker, J., Ayalew, D. & Menzies, M., 2002. Matching conjugate volcanic rifted margins:

40Ar/39Ar chronostratigraphy of pre- and syn-rift bimodal flood volcanism in Ethiopia and Yemen, *Earth planet. Sci. Lett.,* **198,** 289–306.

VanDecar, J. & Crosson, R., 1990. Determination of teleseismic relative phase arrival times using multi-channel cross-correlation and least squares, *Bull. seism. Soc. Am.,* **80**(1), 150–169.

Watts, A.B. & Stewart, J., 1998. Gravity anomalies and segmentation of the continental margin offshore West Africa, *Earth planet. Sci. Lett.,* **156,** 239–252.

Wolfenden, E., Ebinger, C., Yirgu, G., Deino, A. & Ayalew, D., 2004. Evolution of the northern main Ethiopian rift: birth of a triple junction, *Earth planet. Sci. Lett.,* **224,** 213–228.

Worzel, J., 1968. Advances in marine geophysical research of continental margins, *Can. J. Earth Sci.,* **5,** 963–983.

Yuen, G.A., Cadek, O., van Keken, P., Reuteler, D.M., Kyvalova, H. & Schroeder, B.R., 1996. Combined results from mineral physics, tomography and mantle convection and their implications on global geodynamics, in *Seismic modelling of Earth structure,* pp. 463–505, ed. Editrice Compositori, Bologna.

Zeyen, H. & Achauer, U., 1997. Joint inversion of teleseismic delay times and gravity anomaly data for regional structures: theory and synthetic examples, in *Upper Mantle Heterogeneities from Active and Passive Seismology,* pp. 155–168.